Numerical Heat Transfer, Part B, 39:61–78, 2001

1040-7790/01 $12.00 + .00

ON INCOMPRESSIBLE BUOYANCY FLOW BENCHMARKING

Andrej Horvat and Ivo Kljenak
"Jožef Stefan" Institute, Ljubljana, Slovenia

Jure Marn
University of Maribor, Maribor, Slovenia

Nowadays, the use of computational fluid dynamics (CFD) codes has become routine, although there are still some unresolved basic issues. The crucial step in the testing of numerical codes is benchmarking. Accurate solutions of benchmarks represent reference points for code development. As studies have revealed, the already existing benchmarks for natural-convection flows do not satisfactorily validate numerical codes. The authors propose the advection of a hot rectangular plume in a cold fluid placed in a rectangular cavity as a new benchmark for incompressible buoyancy flows. Our attention was focused on low-viscosity flows at zero thermal diffusivity. Together with the benchmark's configuration, the results of numerical calculations are presented to serve as a reference point for further investigations.

1. INTRODUCTION

Computational modeling of fluid behavior has become a dominant tool for analysis and design of industrial installations, transport vehicles, power-generating plants, ventilation, and air conditioning installations. This rapid development was promoted by extreme progress in computational power. Also, numerical algorithms were successively improved over the years. During the past 15 years computational fluid dynamics (CFD) was transformed from research codes used within research institutions into commercial codes such as CFX, Fluent, Fidap, Nekton, Phoenics, STAR-CD, etc. Nowadays, the use of CFD codes has become routine, although there are still some unresolved basic issues.

In a modeling procedure, the physical behavior of a fluid is formulated with mathematical expressions. Although basic equations of fluid motion have been formulated since Navier [1] and Stokes [2], different kinds of flows require specific modifications of the basic equations. The scope and the complexity of problems are so wide that they require classification of problems and consequently equation

Received 28 September 1999; accepted 25 September 2000.

The authors wish to thank the anonymous reviewers for their valuable comments. The financial support of the Ministry of Science and Technology of the Republic of Slovenia is also gratefully acknowledged.

Address correspondence to Andrej Horvat, Reactor Engineering Division, "Jožef Stefan" Institute, Jamova 39, SI-1111, Ljubljana, Slovenia. E-mail: andrej.horvat@ijs.si

NOMENCLATURE

g	gravitational acceleration	$\mathbf{v}$	velocity
Gr	Grasshof number	V	velocity scale
h	temperature	γ	area of finite-volume boundary
H	temperature scale	δ	increment
i	finite-volume boundary interface	Δ	finite difference
n	iteration index	ϑ	finite-volume boundary velocity
p	pressure	θ	"smoothness" coefficient
P	pressure scale	μ	dynamic viscosity
Pr	Prandtl number	ν	kinematic viscosity
q	kinetic energy	υ	thermal diffusivity
r	position vector	ρ	density
Re	Reynolds number	ϕ	superbee limiter
RHS	right hand side of equation	Φ	dimensionless viscosity
t	time	ω	finite volume
t_0	simulation time interval	Ω	simulation domain
T	time scale, simulation time interval		

simplification based on flow regimes. As the regimes of fluid motion are different, the resulting equations can be parabolic, elliptic, hyperbolic, or something in between. Because of this variety of the equations' characteristics, the numerical algorithms to solve the equations are not general but rather specific and case-dependent. The simplification of resulting mathematical equations, in order to be able to obtain a solution, also represents a constant threat of introducing conceptional modeling errors [3].

In many cases, numerical tools are required for solving the equations. Development and usage of numerical algorithms are typically associated with truncation errors, consistency, stability, and convergence. These terms are well explained by Hirsch [4] and will not be discussed further here.

Results of computational models should be extensively verified to prevent conceptional modeling errors, and validated to assure consistency of numerical schemes. The crucial role in this process is "benchmarking," whereby the results of various numerical codes applied to the same standard problem (called a benchmark) are compared. Reference results can include an analytical solution, experimental, or reliable numerical results. In general, it is important for benchmark problems to have a simple geometric arrangement, to be experimentally and computationally feasible (see Leong et al. [5]), as well as widely recognized and accepted. Accurate solutions of benchmarks represent reference points for a code development [6]. If a numerical code accurately predicts benchmark solutions, it may be considered safe to apply the same code to similar problems for which no comparable results exist.

Extensive use of CFD in the aerospace industry resulted in extensive testing of numerical schemes for the Euler equation and the convection-diffusion equation in one- or two-dimensional domains. As a benchmark configuration, a simple step or box function has been widely used (e.g., [7, 8]). In the case of compressible fluid flow, a pressure step function (a shock tube) has been used as a benchmark problem (e.g., [9]).

For incompressible fluid flow, benchmark problems primarily give a steady-state solution. In the case of forced convection of incompressible fluid, Freitas [10] and Rodi et al. [11] defined a horizontal boundary-layer flow, a channel flow, a lid-driven cavity, a geometric step, and a flow past a body (a cylinder or a box) as benchmark problems for commercial CFD codes. In the case of natural convection of incompressible fluid, Hanjalić [12] proposed a vertical boundary layer, a vertical slab, a bottom-heated fluid layer, a side-heated square cavity, a bottom-heated square cavity, and a horizontal annulus as appropriate test cases.

As our studies revealed, already-existing benchmarks for incompressible flow do not satisfactory validate computational models and also do not reveal usual coding errors. Usually, they give information on steady-state conditions, which reflect only a balance between forces in fluid flow. For these reasons, we propose a new benchmark problem for testing computational models of incompressible buoyancy flows, as well as the correctness of the corresponding computer code. Together with the benchmark's configuration, results of initial two-dimensional calculations are also presented.

2. GEOMETRIC CONFIGURATION

As a benchmark problem particularly suited for testing computational models of incompressible buoyancy flow, we propose the advection of a hot rectangular plume in a cold fluid placed in a rectangular cavity. An initial geometric arrangement is shown in Figure 1. Although some experimental work was already done for a spherical plume by Kotsovinos [13], a rectangular shape of the plume was chosen to avoid additional discretization errors, which could arise in cylindrical and spherical geometries. The configuration of the proposed benchmark was similar to the single-rising-bubble test, which was generally accepted in the multiphase-flow community. Some early experimental work on this subject was presented by Bhaga and Weber [14].

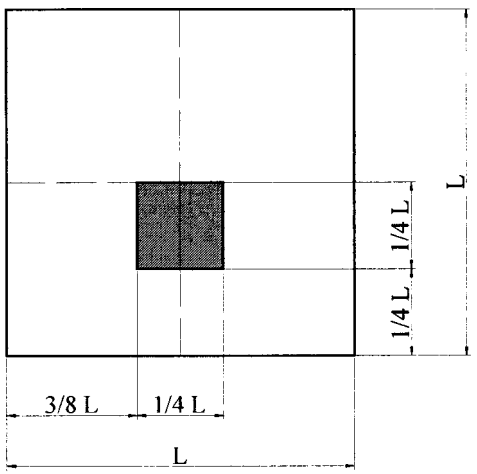

Figure 1. Geometric arrangement of the benchmark problem.

The thermal plume is composed of the same fluid as the surrounding cold fluid. Initially, it is placed in the lower half of the simulation domain. The plume has a dimensionless temperature 1, whereas the surrounding liquid has a dimensionless temperature 0. The fluid is initially considered at rest.

On all boundaries of the simulation domain, no-slip boundary conditions were defined for the fluid velocity, whereas for the temperature, adiabatic boundary conditions were prescribed.

Due to the transient nature of the buoyancy flow in the case presented (the plume will rise and spread), the proposed benchmark configuration is much more selective than other benchmark problems. The results are especially sensitive to numerical scheme errors and to inconsistencies in boundary conditions on the cavity walls. For the proposed benchmark problem, the modeling procedure and the initial results from numerical simulations are presented below.

3. MATHEMATICAL MODEL

As the fluid is considered incompressible, fluid motion and heat transfer can be described with the following mass (1), momentum (2), and energy (3) conservation equations:

$$\int_\gamma \mathbf{v} \cdot d\gamma = 0 \qquad \forall t \in \mathrm{T} \wedge \forall \mathbf{r} \in \overline{\Omega} \tag{1}$$

$$\rho \frac{\partial}{\partial t} \int_\omega \mathbf{v}\, d\omega + \rho \int_\gamma (\mathbf{v} \otimes \mathbf{v}) \cdot d\gamma = -\int_\gamma p\, d\gamma + \int_\gamma \mu \nabla \mathbf{v} \cdot d\gamma + \int_\omega \rho \mathbf{g}\, d\omega \qquad \forall t \in \mathrm{T} \wedge \forall \mathbf{r} \in \overline{\Omega} \tag{2}$$

$$\frac{\partial}{\partial t} \int_\omega h\, d\omega + \int_\gamma (\mathbf{v}h) \cdot d\gamma = \int_\gamma v \nabla h \cdot d\gamma \qquad \forall t \in \mathrm{T} \wedge \forall \mathbf{r} \in \overline{\Omega} \tag{3}$$

To reduce the number of free parameters in the calculations and to simplify the comparison of results, Eqs. (1), (2), and (3) were transformed into dimensionless form. Assuming a small temperature difference between the plume and the surrounding fluid, the Boussinesq approximation was used to include buoyancy forces:

$$\int_\gamma \mathbf{v} \cdot d\gamma = 0 \tag{4}$$

$$\frac{\partial}{\partial t} \int_\omega \mathbf{v}\, d\omega + \int_\gamma (\mathbf{v} \otimes \mathbf{v}) \cdot d\gamma = -\int_\gamma p\, d\gamma + \int_\gamma \frac{1}{\mathrm{Re}} \nabla \mathbf{v} \cdot d\gamma + \int_\omega \frac{\mathrm{Gr}}{\mathrm{Re}^2} h\, d\omega \tag{5}$$

$$\frac{\partial}{\partial t} \int_\omega h\, d\omega + \int_\gamma (\mathbf{v}h) \cdot d\gamma = \int_\gamma \frac{1}{\mathrm{Pr}\,\mathrm{Re}} \nabla h \cdot d\gamma \tag{6}$$

As scaling factors, the height of the simulation domain L, the time T, the initial density ρ, the kinematic viscosity v, the thermal diffusivity υ, and the volumetric thermal dilatation β were used. With this scaling procedure, the following system

parameters were defined:

$$\begin{aligned} &\text{Reynolds number:} && \mathrm{Re} = \frac{VL}{\nu} \\ &\text{Prandtl number:} && \mathrm{Pr} = \frac{\nu}{\upsilon} \\ &\text{Grasshof number:} && \mathrm{Gr} = \frac{\beta g H L^3}{\nu^2} \end{aligned} \tag{7}$$

To test the most severe conditions, thermal diffusion was dropped from the energy conservation equation (6):

$$\frac{1}{\mathrm{Pr}\,\mathrm{Re}} = 0 \tag{8}$$

This prescription ensures thermal energy conservation in the plume, although its shape is deformed due to fluid convection. Therefore, any energy losses from the plume during numerical simulations were caused only by numerical scheme diffusion. Without loss of generality, the buoyancy-term parameter was set to 1:

$$\frac{\mathrm{Gr}}{\mathrm{Re}^2} = 1 \tag{9}$$

The last assumption, which can be also found in Wörner et al. [15], fully defines the time scale T and the velocity scale V used in the scaling procedure. As a consequence, conservation equations (4)–(6) assume the following forms:

$$\int_\gamma \mathbf{v} \cdot d\gamma = 0 \tag{10}$$

$$\frac{\partial}{\partial t}\int_\omega \mathbf{v}\, d\omega + \int_\gamma (\mathbf{v} \otimes \mathbf{v}) \cdot d\gamma = -\int_\gamma p\, d\gamma + \Phi \int_\gamma \nabla \mathbf{v} \cdot d\gamma + \int_\omega h\, d\omega \tag{11}$$

$$\frac{\partial}{\partial t}\int_\omega h\, d\omega + \int_\gamma (\mathbf{v}h) \cdot d\gamma = 0 \tag{12}$$

where the dimensionless viscosity $1/\mathrm{Re} = \Phi$ is the only remaining free parameter.

In our experience, convection is the most problematic and therefore challenging part of numerical modeling; hence, our attention was focused on low-viscosity flows. The proposed tests were thereby conducted for values of Φ set to 0.1, 0.01, 0.001, 0.0001, and 0.0.

4. NUMERICAL METHODS

Although our purpose was not to develop a specific numerical scheme but to propose an optimal benchmark configuration, we believe that the numerical methods used in our calculations should be briefly described in order to provide a complete picture of the proposed problem.

4.1. Convection and Diffusion Fluxes

The conservation equations (10)–(12) were discretized in two dimensions according to the finite-volume method. A fully staggered arrangement for grid points

was applied. Examples [Eqs. (13)–(18)] for different spatial discretization techniques for convection terms are given only for the energy equation (12). We tested various combinations of central-symmetric [Eq. (13)], upwind [Eq. (14)], Lax-Wendroff [Eq. (15)], and high-resolution schemes [Eq. (16)]. With the high-resolution method, the so-called superbee limiter [Eq. (18)] was used as defined by LeVeque [16].

$$\int_\gamma (\mathbf{v}h)\cdot d\gamma = \sum_i \vartheta_{\mathbf{r}_i}\ h_{\mathbf{r}_i}\cdot\gamma_{\mathbf{r}_i} \tag{13}$$

$$\int_\gamma (\mathbf{v}h)\cdot d\gamma = \sum_i \left(\vartheta^+_{\mathbf{r}_i} h_{\mathbf{r}_i-\delta\mathbf{r}_i} + \vartheta^-_{\mathbf{r}_i}\ h_{\mathbf{r}_i+\delta\mathbf{r}_i}\right)\cdot\gamma_{\mathbf{r}_i} \tag{14}$$

$$\int_\gamma (\mathbf{v}h)\cdot d\gamma = \sum_i \vartheta_{\mathbf{r}_i}\left[h_{\mathbf{r}_i} - \frac{1}{2}\delta t(\nabla\cdot\mathbf{v}h)_{\mathbf{r}_i}\right]\cdot\gamma_{\mathbf{r}_i} \tag{15}$$

$$\int_\gamma (\mathbf{v}h)\cdot d\gamma = \sum_i \left[\begin{array}{c}(1-\varphi_{\mathbf{r}_i})\left(\vartheta^+_{\mathbf{r}_i}\ h_{\mathbf{r}_i-\delta\mathbf{r}_i} + \vartheta^-_{\mathbf{r}_i}\ h_{\mathbf{r}_i+\delta\mathbf{r}_i}\right)\\ +(\varphi_{\mathbf{r}_i})\vartheta_{\mathbf{r}_i}\left(h_{\mathbf{r}_i} - \frac{1}{2}\delta t(\nabla\cdot\mathbf{v}h)_{\mathbf{r}_i}\right)\end{array}\right]\cdot\gamma_{\mathbf{r}_i} \tag{16}$$

$$\vartheta_{\mathbf{r}_i} = 0.5\left(\mathbf{v}_{\mathbf{r}_i-\delta\mathbf{r}_i} + \mathbf{v}_{\mathbf{r}_i+\delta\mathbf{r}_i}\right) \qquad \vartheta^+_{\mathbf{r}_i} = \max\left(0, \vartheta_{\mathbf{r}_i}\right) \qquad \vartheta^-_{\mathbf{r}_i} = \min\left(0, \vartheta_{\mathbf{r}_i}\right) \tag{17}$$

$$\theta_{\mathbf{r}_i} = \frac{h_{\mathbf{r}_i'+\delta\mathbf{r}_i} - h_{\mathbf{r}_i'}}{h_{\mathbf{r}_i+\delta\mathbf{r}_i} - h_{\mathbf{r}_i}} \qquad \mathbf{r}_{i'} = \mathbf{r}_i - \mathrm{sign}(\vartheta_{\mathbf{r}_i})\delta\mathbf{r}_i \qquad \varphi_{\mathbf{r}_i} = \max[0,\ \min(1, 2\theta), \min(\theta, 2)]_{\mathbf{r}_i} \tag{18}$$

We found out that the high-resolution scheme [Eq. (16)] with the superbee limiter [Eq. (18)] applied to the momentum [Eq. (11)] as well as to the energy conservation equation [Eq. (12)] produces the most physically reasonable and accurate results. Although some modifications of the high-resolution discretization were necessary, accuracy and stability are a consequence of controlled numerical diffusion of this scheme compared to the other schemes tested. Due to the high selectivity of the proposed benchmark problem, other numerical schemes used for the convection terms discretization produced large local deviations.

In all cases, the momentum diffusion term [Eq. (11)] was discretized central-symmetrically:

$$\Phi\int_\gamma \nabla\mathbf{v}\cdot d\gamma = \Phi\sum_i \frac{\mathbf{v}_{\mathbf{r}_i+\delta\mathbf{r}_i} - \mathbf{v}_{\mathbf{r}_i-\delta\mathbf{r}_i}}{2\delta\mathbf{r}_i}\cdot\gamma_{\mathbf{r}_i} \tag{19}$$

4.2. Time Integration

For time integration of the momentum (11) and energy (12) conservation equations, we tested the explicit Euler method:

$$\frac{h^{n+1} - h^n}{\Delta t^n} = \mathrm{RHS}^n \tag{20}$$

and the two-step Adam-Bashforth method:

$$\frac{h^{n+1} - h^n}{\Delta t^n} = \mathrm{RHS}^n + 0.5\,\Delta t^n\frac{\left(\mathrm{RHS}^n - \mathrm{RHS}^{n-1}\right)}{\Delta t^{n-1}} \tag{21}$$

It should be noted that the derivation of the presented spatial high-resolution scheme [Eq. (16)] is not independent from a time-discretization procedure. For that reason, the high-resolution spatial discretization scheme can be combined only with the explicit Euler method.

4.3. Pressure Calculation

The pressure calculation was treated in accordance with the projection method as proposed by Bell et al. [17]. In this way, the solenoidal velocity field $\mathbf{v}$ was decomposed into the non-divergence-free velocity field $\mathbf{v}^*$ and the pressure gradient. First, the auxiliary vector field $\mathbf{v}^*$ was computed from Eq. (22):

$$\mathbf{v}^* = \Delta t^n \left(\mathrm{RHS}^{n+1/2}\right) + \mathbf{v}^n \tag{22}$$

Then, Eq. (22) was combined with the mass conservation Eq. (10) in order to obtain the Poisson equation for the pressure. In our case, the Poisson equation was solved by implementing a direct Poisson solver, to take advantage of its high accuracy. At the end, the pressure gradient was subtracted from the intermediate velocity:

$$\mathbf{v}^{n+1} = \mathbf{v}^* - \frac{\Delta t^n}{\omega} \sum_i p_{\mathbf{r}_i} \gamma_{\mathbf{r}_i} \tag{23}$$

Numerical calculations for the proposed benchmark problem were performed on 32×32, 64×64, and 128×128 grid points to check the consistency of results. Although different numerical schemes and methods were tested, only the results obtained with the high-resolution method are presented.

5. RESULTS AND DISCUSSION

The time intervals of numerical simulations were adapted to accommodate different viscosity cases. The simulations ended when the thermal plume reached its highest position. For $\Phi = 0.1$ the dimensionless simulation time t_0 was 50, for $\Phi = 0.01$ t_0 was 5, for $\phi = 0.001$ t_0 was 4, for $\Phi = 0.0001$ t_0 was 3.5, and for $\Phi = 0$ t_0 was 3.

5.1. Thermal Field

Figure 2 shows development of the thermal plume at viscosity $\Phi = 0.1$. As the buoyancy force moves the fluid, the shear stresses on the walls strongly increase. Due to the high viscosity compared to the other cases, the effect of wall shear becomes dominant shortly after the simulation start. This wall effect decreases the velocity of the moving thermal plume. Also, high shear stresses cause the thermal plume to stay compact during the entire simulation time. Even the corners of the thermal plume remain visible until the end of the simulation.

As the viscosity is reduced, the thermal plume velocity increases (Figure 3). The corners are not as evident as in the previous case. During the simulation, the formation of two wings (left and right) can be observed in the still compact plume.

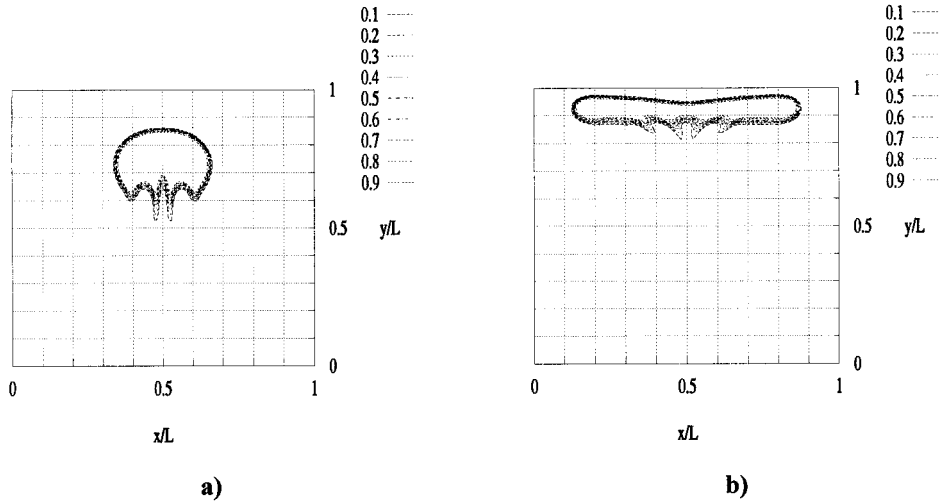

Figure 2. Temperature field at $\Phi = 0.1$: (*a*) $t = 0{,}25t_0$; (*b*) $t = t_0$ (figures indicate temperature values corresponding to isotherms).

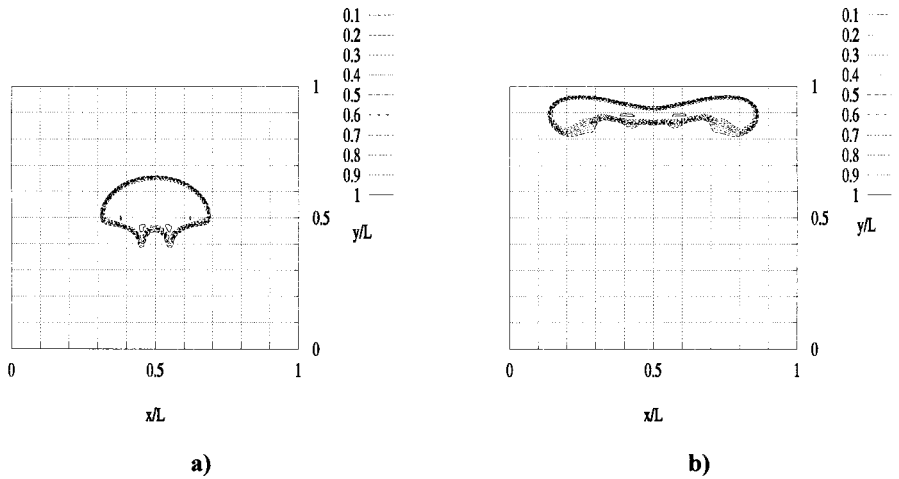

Figure 3. Temperature field at $\Phi = 0.01$: (*a*) $t = 0{,}25t_0$; (*b*) $t = t_0$.

Figure 3 also reveals small numerical overestimates of the temperature field marked with contour 1.0, placed symmetrically in the thermal plume.

At viscosity $\Phi = 0.001$ (Figure 4), the formation of the two wings is clearly evident. The velocity of the plume is further increased and becomes more uniform throughout the simulation time. As the thermal plume develops, the Rayleigh-Taylor instabilities cause local deformation of the plume in a fractal-like manner.

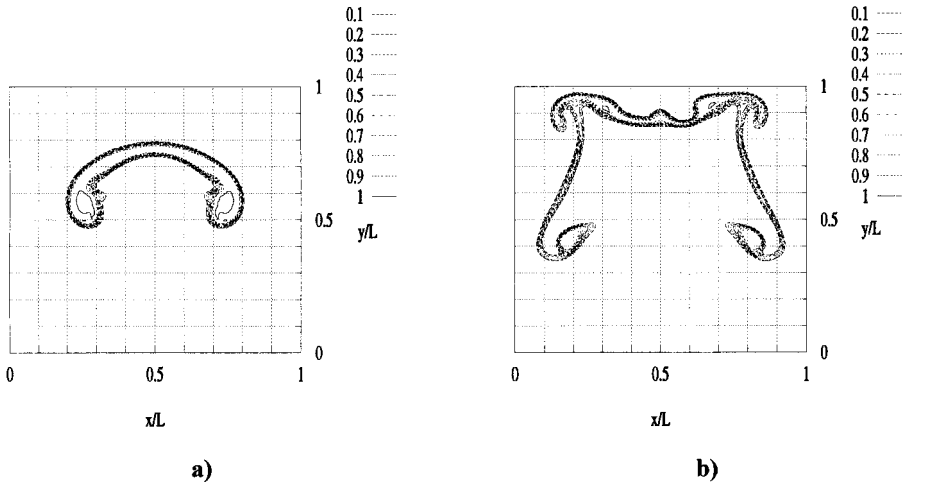

Figure 4. Temperature field at $\Phi = 0.001$: (*a*) $t = 0{,}5t_0$; (*b*) $t = t_0$.

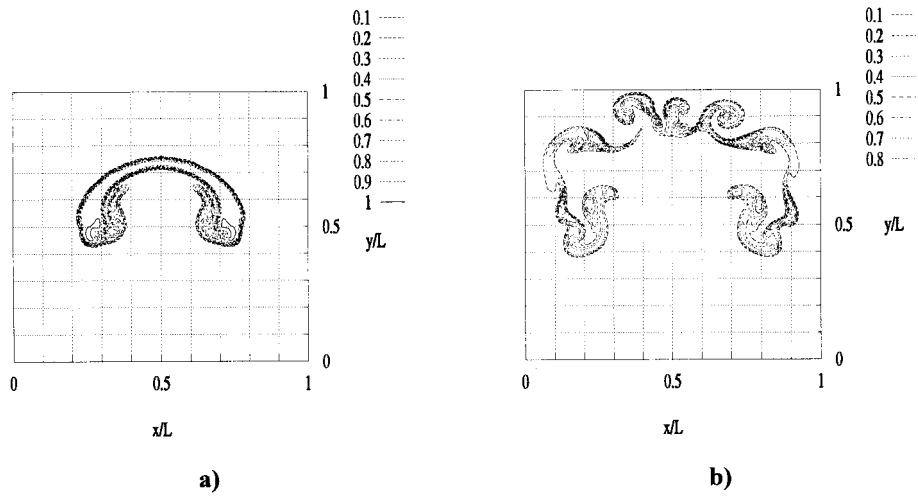

Figure 5. Temperature field at $\Phi = 0.0001$: (*a*) $t = 0{,}5t_0$; (*b*) $t = t_0$.

At viscosity $\Phi = 0.0001$ (Figure 5), the wall shear stress plays only a minor role in the thermal plume movement. The buoyancy force increases the velocity of the plume almost to the end of the simulation time. Deformations due to the local Rayleigh-Taylor instabilities become stronger. The reduction of the fluid motion scale due to instabilities also causes asymmetrical behavior.

At zero viscosity (Figure 6), there is no stress present in the fluid and the scale of fluid motion is infinitely small, as described by Chandrasekhar [18]. Only the stresses caused by the numerical diffusivity of the discretization scheme balance the

buoyancy. The numerical approximation is unable to capture the whole spectrum of scales due to finite grid spacing. For this reason, numerical simulations of buoyancy flows at zero viscosity do not have any physical meaning. Namely, the error caused by the finite grid spacing will grow throughout the numerical simulation, producing results far away from realistic physical conditions.

5.2. Induced Velocity Field

The velocity field is composed mainly from two counterrotating vortices. Figures 7–11 show the velocity fields as vector plots normalized with the highest velocity in each case. This does not give an accurate representation of the absolute velocity

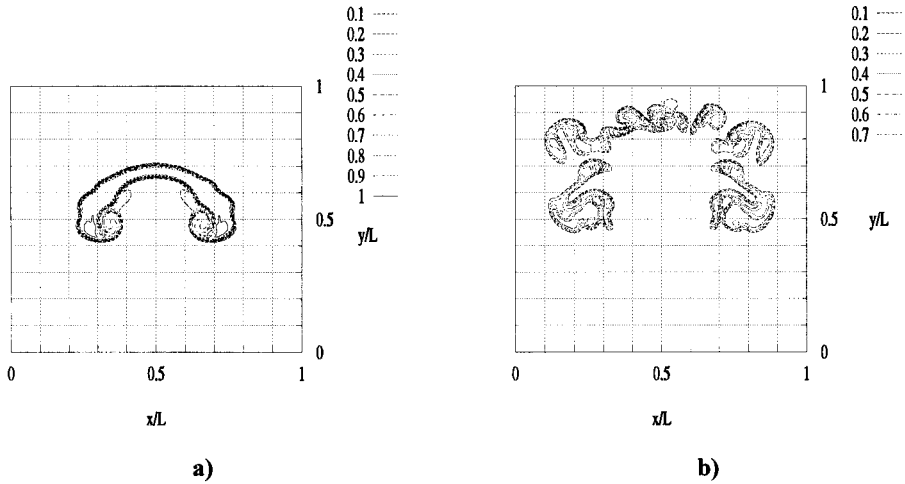

Figure 6. Temperature field at $\Phi = 0.0$: (*a*) $t = 0{,}5t_0$; (*b*) $t = t_0$.

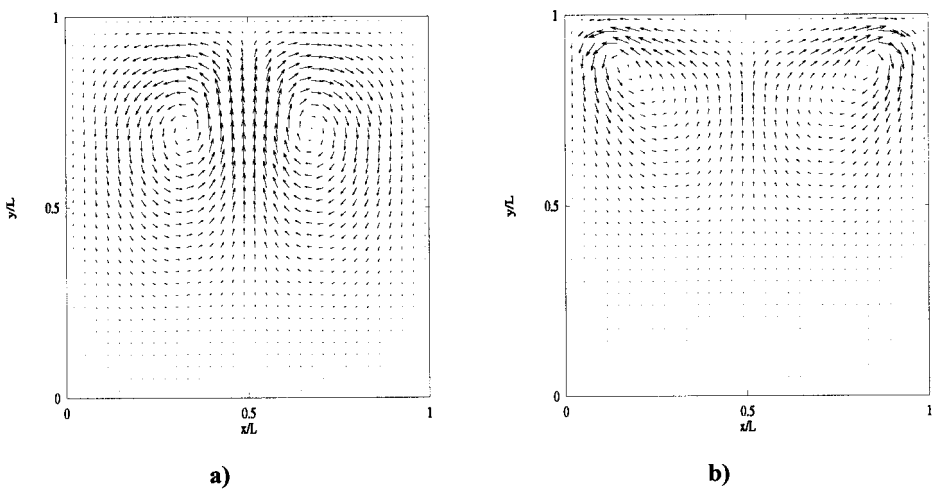

Figure 7. Velocity field at $\Phi = 0.1$: (*a*) $t = 0{,}25t_0$; (*b*) $t = t_0$.

but rather a good qualitative information about the circulation pattern. Also, for the clarity of the presentation, only every fourth grid point with the corresponding velocity vector is shown.

Figure 7 presents the velocity field at viscosity $\Phi = 0.1$. Due to the high viscosity, the vortices are symmetrical and the distance between the two vortex centers is small. As the plume deforms towards the end of the simulation, the vortices travel apart and the velocity decreases due to the wall shear stresses.

At viscosity $\Phi = 0.01$ (Figure 8), the symmetry of the circulation pattern is still preserved. At the end of the simulation, Figure 8*b* reveals stretching of the primary

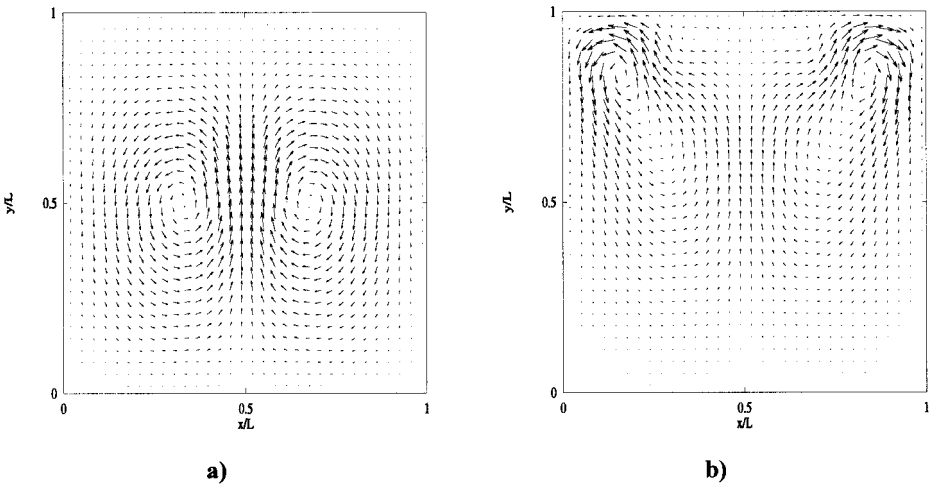

Figure 8. Velocity field at $\Phi = 0.01$: (*a*) $t = 0{,}25t_0$; (*b*) $t = t_0$.

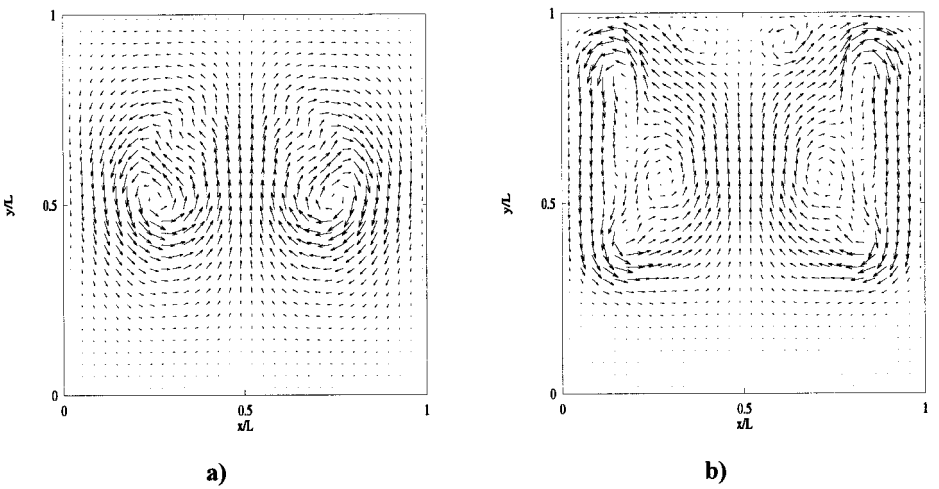

Figure 9. Velocity field at $\Phi = 0.001$: (*a*) $t = 0{,}5t_0$; (*b*) $t = t_0$.

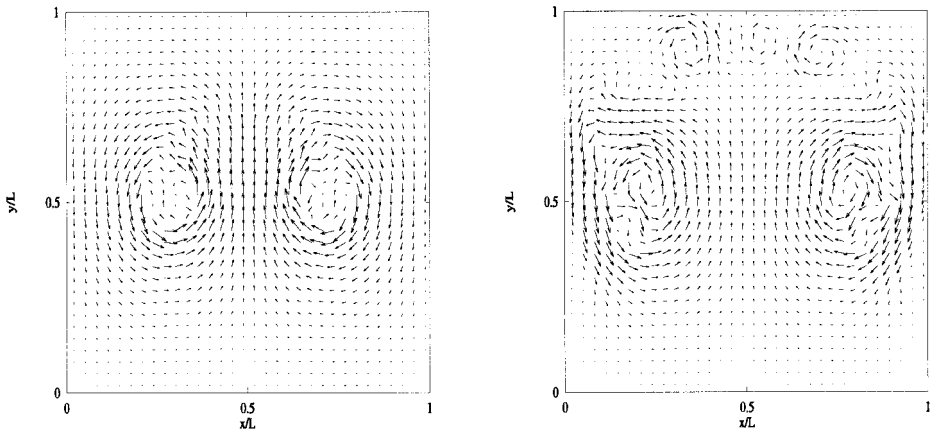

Figure 10. Velocity field at $\Phi = 0.0001$: (*a*) $t = 0.5t_0$; (*b*) $t = t_0$.

vortices from the upper corners toward the center of the simulation domain and appearance of a small secondary vortex pair at the upper boundary.

At viscosity $\Phi = 0.001$ (Figure 9), the thermal plume deformation already has a strong influence on the velocity field. The vortices' shape becomes irregular and the vortex centers are more apart than in the previous cases. The general circulation pattern, although preserved at the end of the simulation (Figure 9*b*), is unstable and composed from three different vortex pairs.

At viscosity $\Phi = 0.0001$ (Figure 10), the velocity scale is smaller than the presentation scale (four grid spaces). Figure 10*a* already reveals the multivortex structure inside two counterrotating vortices. At the end of the simulation (Figure 10*b*), the circulation symmetry is preserved only on the "macroscopic" level, whereas the general circulation pattern is broken into more circulation cells.

As already noted, the scale of fluid motion is infinitely small at zero viscosity. Due to local instabilities caused by negative temperature gradients in the vertical direction, the circulation pattern is broken into fragments as shown in Figures 11*a* and 11*b*. Although the general circulation pattern is still preserved on the macroscopic level, more detailed investigations reveal a fractal-like structure of vortices at the hot–cold fluid interface.

5.3. Consistency of Numerical Results

To check the consistency of numerical results and the influence of numerical error, the simulations' results were obtained on three different numerical meshes using 32×32, 64×64, and 128×128 grid points. The test results are summarized in Figures 12–16. Figures 12*a*, 13*a*, 14*a*, 15*a*, and 16*a* present a temperature contour 0.75, whereas Figures 12*b*, 13*b*, 14*b*, 15*b*, and 16*b* present a vertical cross section at $x/L = 0.5$ through the temperature field. The figures also show that the selected

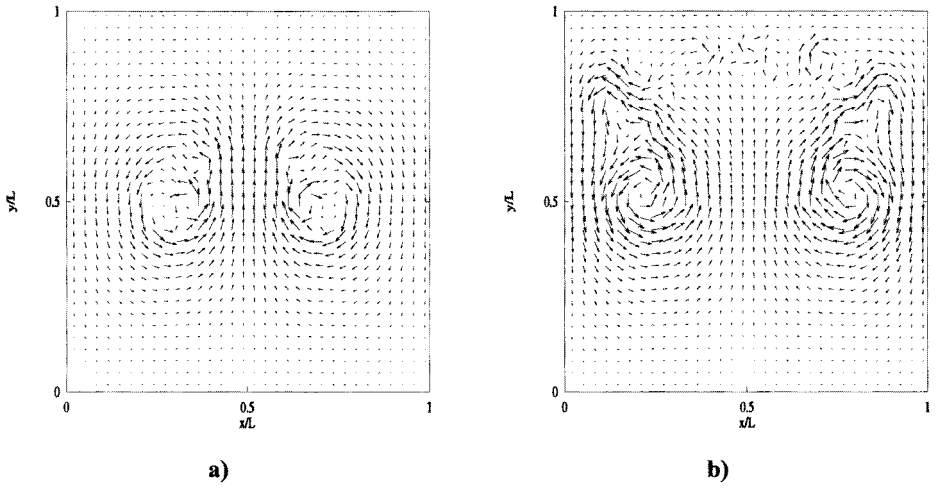

Figure 11. Velocity field at $\Phi = 0.0$: (*a*) $t = 0.5t_0$; (*b*) $t = t_0$.

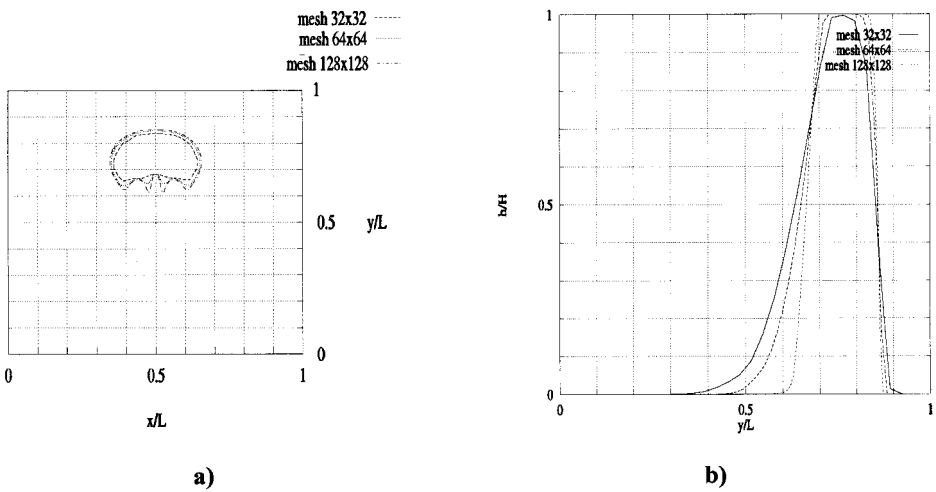

Figure 12. Temperature at $t = 0.25t_0$, $\Phi = 0.1$: (*a*) isotherm $h = 0.75$; (*b*) cross section at $x/L = 0.5$.

numerical scheme, although second-order-accurate, does not exhibit additional numerical oscillations.

Figures 12 and 13 show relatively small differences between results when different numerical meshes are applied. This is due to relatively high viscosity Φ, where the numerical (false) diffusion makes only a small contribution. The numerical drain of momentum and energy from the thermal plume is practically negligible. The thermal energy of the plume stays preserved during the whole simulation interval. Figures 12*b* and 13*b* also reveal that the discretization error is smaller at the front and much larger at the back of the spreading thermal plume. This is a consequence of discretization error odd terms, which change their sign over the thermal plume.

When the viscosity Φ is lower than or equal to 0.001, the numerical mesh resolution is inadequate when only 32×32 or 64×64 grid points are used. As Figures 14, 15, and 16 show, the discrepancies between results are large. Unlike the numerical mesh with 128×128 grid points, where a maximum temperature h is still close to 1, coarser numerical meshes are not able to capture a thin thermal front, which is formed between both wings of the thermal plume (e.g., Figure 14*a*). Together with the numerical drain of momentum and thermal energy, numerical models using 32×32 or 64×64 grid points are able to produce only results with poor accuracy. Due to high sensitivity of the proposed benchmark problem, the differences between a

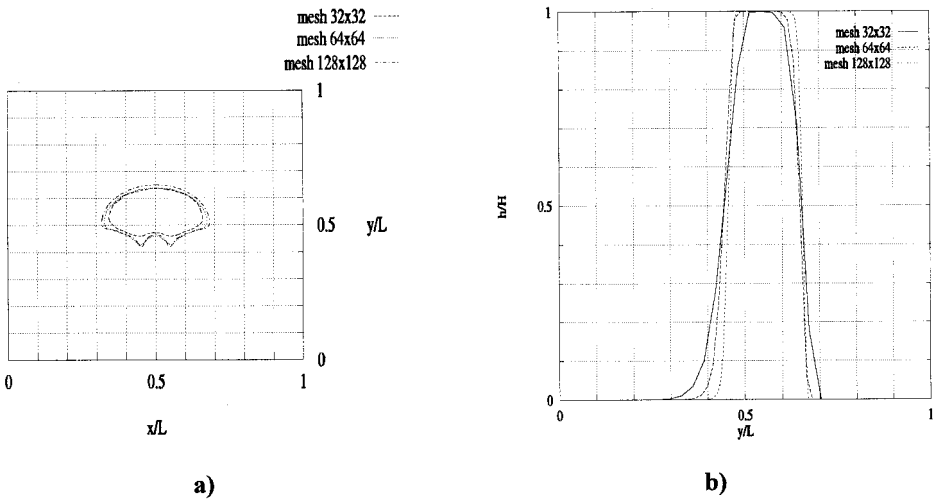

Figure 13. Temperature at $t=0.25t_0$, $\Phi=0.01$: (*a*) isotherm $h=0.75$; (*b*) cross section at $x/L=0.5$.

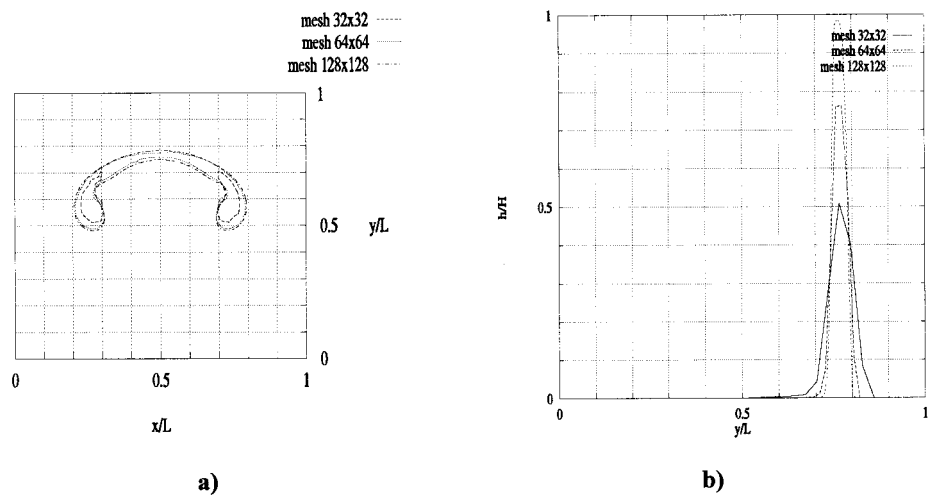

Figure 14. Temperature at $t=0.5t_0$, $\Phi=0.001$: (*a*) isotherm $h=0.75$; (*b*) cross section at $x/L=0.5$.

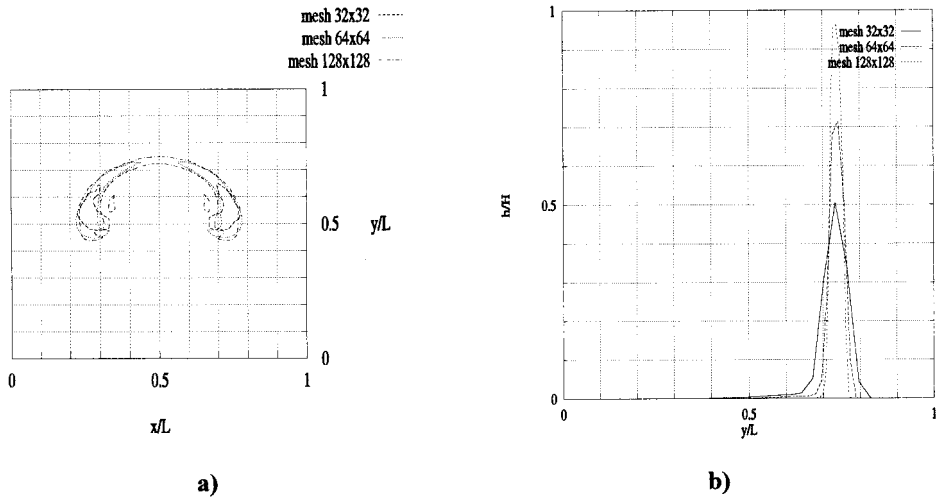

Figure 15. Temperature at $t = 0{,}25t_0$, $\Phi = 0.0001$: (*a*) isotherm $h = 0.75$; (*b*) cross section at $x/L = 0.5$.

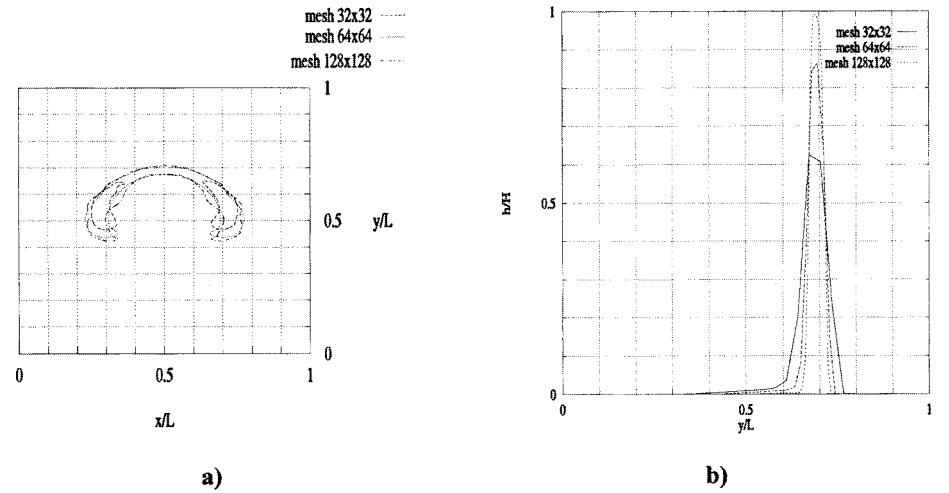

Figure 16. Temperature at $t = 0{,}25t_0$, $\Phi = 0.0$: (*a*) isotherm $h = 0.75$; (*b*) cross section at $x/L = 0.5$.

numerical prediction and physical behavior will only increase along the simulation time interval.

5.4. System Kinetic Energy

During the simulations, the influence of viscosity on the average kinetic energy of the fluid was also observed. The average kinetic energy of the fluid was defined as

$$q(t) = \frac{1}{\Omega} \sum_i \frac{\mathbf{v}(t)^2}{2} \omega_i \tag{24}$$

Again, comparisons between the kinetic energy [Eq. (24)] time distributions were performed for three different densities of numerical meshes using 32×32, 64×64, and 128×128 grid points.

At the high viscosity $\Phi=0.1$ (Figure 17*a*), the average kinetic energy of a fluid particle is low. The system experiences a short ''acceleration'' at the beginning of the simulation interval due to buoyancy. When shear forces prevail, the kinetic energy decreases.

As the viscosity is decreased to $\Phi=0.01$ (Figure 17*b*), the kinetic energy increases. The maximum of the kinetic energy is more than 40 times higher than in the case where the viscosity Φ is 0.1. Lower viscosity also causes weaker shear stresses, which makes the acceleration period of the system much longer.

At viscosity $\Phi=0.001$ (Figure 17*c*), the grid dependence of the results is already observable. The discretization error is large at the average kinetic energy peak value as well as at the end of the simulation time when the thermal plume reaches the upper boundary. Further decreasing of the viscosity increases the kinetic energy, but not as sharply as in the previous case (only for a factor of 2). The reduction of stresses prolongs the ''acceleration'' period of the system.

At viscosity $\Phi=0.0001$ (Figure 17*d*), the peak kinetic energy occurs near the end of the simulation time interval. The position and height of the peak is grid-dependent, revealing insufficient resolution of the numerical meshes with only 32×32 and 64×64 grid points. Although the viscosity is lower than in the previous case for a factor of 10, the kinetic energy increases by only 20%. This indicates that the buoyancy force has a dominant effect on fluid motion.

At zero viscosity (Figure 17*e*), the peak kinetic energy is only slightly increased compared to the previous case. The peak location is moved further toward the end of the simulation time interval. At the end of the simulation, the kinetic energy slightly decreases, due to boundary conditions and numerical diffusivity, which is still present.

6. CONCLUSIONS

The proposed contribution summarizes our efforts to find a suitable numerical algorithm for simulating buoyancy flows. The plethora of different numerical schemes available in the open literature poses the essential question of how to test and reveal conceptual modeling errors, inconsistencies, discretization errore and simple coding errors. We did not succeed in finding a suitable benchmark problem encompassing these elements. As described, we found none of the existing benchmark problems selective enough. This forced us to construct a new benchmark problem for buoyancy flows.

As we are aware of the importance of the benchmarking process during numerical code development and testing, we herein propose a new benchmark problem for validation and verification of buoyancy flow models. During our own calculations, we found it to be very selective, producing large unphysical discrepancies even at small errors in the equation discretization. This enabled us to construct our numerical algorithm for buoyancy flow simulations.

The numerical methods used for the benchmark calculation are described in the article. The numerical calculations were done at zero thermal diffusivity and at selec-

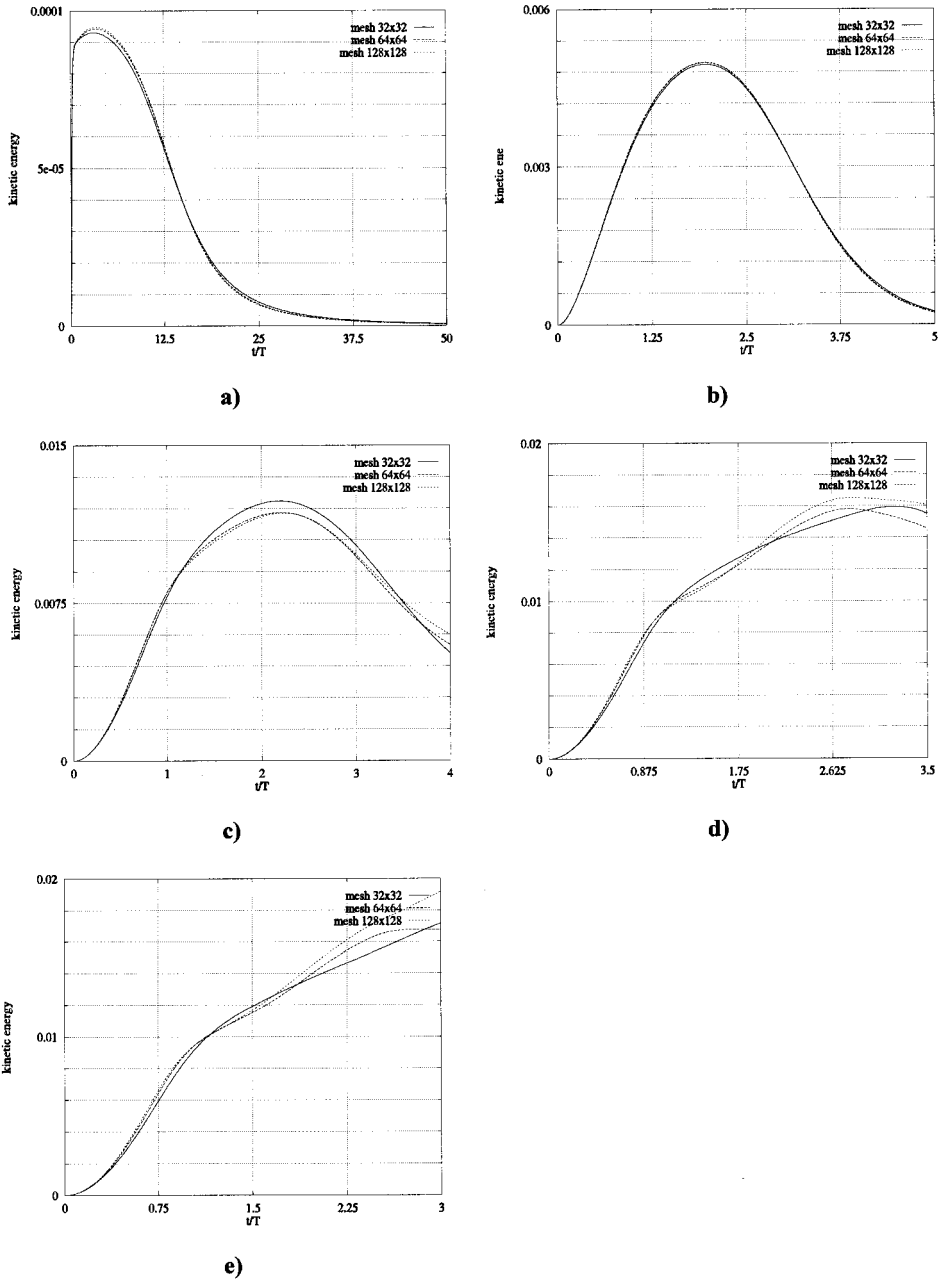

Figure 17. Average kinetic energy of a fluid particle: (*a*) $\Phi = 0.1$; (*b*) $\Phi = 0.01$; (*c*) $\Phi = 0.001$; (*d*) $\Phi = 0.0001$; (*e*) $\Phi = 0.0$.

ted values of viscosity (Φ was 0.1, 0.01, 0.001, 0.0001, and 0). The results are also extensively presented to serve as a reference point for further investigations.

We are aware of the deficiencies of using a two-dimensional model for natural convection, especially at low viscosity. We hope that the model of the proposed benchmark problem will soon be extended and calculated in three dimensions to get more realistic and applicable results.

REFERENCES

1. C. L. M. H. Navier, Mémoire sur les lois du mouvement des fluides, *Mém. Acad. Roy. Sci.*, vol. 6, pp. 389–440, 1823.
2. G. G. Stokes, On Some Cases of Fluid Motion, *Trans. Camb. Phil. Soc.*, vol. 8, p. 105, 1843.
3. P. J. Roache, *Verification and Validation in Computational Science and Engineering*, pp. 23–36. Hermosa Publishers, Albuquerque, NM, 1998.
4. C. Hirsch, *Numerical Computation of Internal and External Flows*, vol. 1, pp. 267–282. Wiley, New York, 1988.
5. W. H. Leong, K. G. T. Hollands, and A. P. Brunger, On a Physical-Realizable Benchmark Problem in Internal Natural Convection, *Int. J. Heat Mass Transfer*, vol. 41, pp. 3817–3828, 1998.
6. W. H. Leong, K. G. T. Hollands, and A. P. Brunger, Experimental Nusselt Numbers for a Cubical Cavity Benchmark Problem in Natural Convection, *Int. J. Heat Mass Transfer*, vol. 42, pp. 1979–1989, 1999.
7. W. Shzz, M.-H. Chen, R. Mittal, and H. S. Udaykumar, On the Supression of Numerical Oscillations Using a Non-linear Filter, *J. Comput. Phys.*, vol. 102, pp. 49–62, 1992.
8. R. LeVeque, High Resolution Finite Volume Method on Arbitrary Grids via Wave Propagation, *J. Comput. Phys.*, vol. 78, pp. 36–63, 1988.
9. J. Falcovitz and M. Ben-Artzi, Recent Developments of the GRP Method, *Jpn. Soc. Mech. Eng. Int. J.*, vol. 38, no. 4, pp. 497–517, 1995.
10. C. J. Freitas, Perspective: Selected Benchmarks from Commercial CFD Codes, *ASME J. Fluid Eng.*, vol. 117, pp. 208–218, 1995.
11. W. Rodi, J. H. Ferziger, M. Breuer, and M. Pourquié, Status of Large Eddy Simulation: Results of Workshop, *ASME J. Fluid Eng.*, vol. 119, pp. 248–262, 1997.
12. K. Hanjali, Achievements and Limitations in Modeling and Computation of Buoyant Turbulent Flows and Heat Transfer, *Proc. 10th Int. Heat Transfer Conf.*, vol. 1, pp. 1–18, Brighton, U.K., 1994.
13. N. E. Kotsovinos, Turbulence Spectra in Free Convection Flow, *Phys. Fluids A*, vol. 3, no. 1, pp. 163–167, 1991.
14. D. Bhaga and M. E. Weber, Bubbles in Viscous Liquids: Shapes, Wakes and Velocities, *J. Fluid Mech.*, vol. 105, pp. 61–85, 1981.
15. M. Wörner, M. Schmidt, and G. Grötzbach, Direct Numerical Simulation of Turbulence in an Internally Heated Convective Fluid Layer and Implications for Statistical Modeling, *J. Hyd. Research*, vol. 35, no. 6, pp. 773–797, 1997.
16. R. J. LeVeque, *Numerical Methods for Conservation Laws*, 2d ed., pp. 176–183. Birkhäuser Verlag, Basel, 1992.
17. J. B. Bell, P. Colella, and H. M. A. Glaz, Second Order Projection Method for the Incompressible Navier-Stokes Equation, *J. Comput. Phys.*, vol. 2, pp. 257–283, 1989.
18. S. Chandrasekhar, *Hydrodynamic and Hydromagnetic Stability*, 3d ed., p. 433. Dover, New York, 1981.